Clustering of Marine-Debris- and *Sargassum*-Like Drifters Explained by Inertial Particle Dynamics

P. Miron[1] , **M. J. Olascoaga[2]** , **F. J. Beron-Vera[1]** , **N. F. Putman[3]** , **J. Triñanes[4,5,6]** , **R. Lumpkin[4]** , and **G. J. Goni[4]**

[1]Department of Atmospheric Sciences, RSMAS, University of Miami, Miami, FL, USA, [2]Department of Ocean Sciences, RSMAS, University of Miami, Miami, FL, USA, [3]LGL Ecological Research Associates, Inc., Bryan, TX, USA, [4]Atlantic Oceanographic and Meteorological Laboratory, NOAA, Miami, FL, USA, [5]Cooperative Institute for Marine and Atmospheric Studies, University of Miami, Miami, FL, USA, [6]CRETUS, Universidade de Santiago de Compostela, Santiago, Spain

Abstract Drifters designed to mimic floating marine debris and small patches of pelagic *Sargassum* were satellite tracked in four regions across the North Atlantic. Though subjected to the same initial conditions at each site, the tracks of different drifters quickly diverged after deployment. We explain the clustering of drifter types using a recent Maxey-Riley theory for surface ocean inertial particle dynamics applied on multidata-based mesoscale ocean currents and winds from reanalysis. Simulated trajectories of objects at the air-sea interface are significantly improved when represented as inertial (accounting for buoyancy and size), rather than as perfectly Lagrangian (fluid following) particles. Separation distances between simulated and observed trajectories were substantially smaller for debris-like drifters than for *Sargassum*-like drifters, suggesting that additional consideration of its physical properties relative to fluid velocities may be useful. Our findings can be applied to model variability in movements and distribution of diverse objects floating at the ocean surface.

Plain Language Summary Predicting the fate of floating matter requires one to recognize that they respond differently than Lagrangian (i.e., infinitesimally small, neutrally buoyant) particles to the action of surface currents and winds. Indeed, the Maxey-Riley equation of fluid mechanics—a Newton second-law-type ordinary differential equation—shows that even the motion of seemingly small neutrally buoyant particles immersed in a fluid in motion can substantively deviate from that of Lagrangian particles. The Maxey-Riley equation has been recently extended to account for the combined effects of ocean current and wind drag on finite-size particles floating at the ocean surface. We show here that the paths of drifters that mimic marine debris and small *Sargassum* patches cluster according to their inertial characteristics consistent with the Maxey-Riley theory.

1. Introduction

Floating matter of a very diverse nature ranging from microplastics (Cózar et al., 2014) to larger objects (Maximenko et al., 2019; Van Sebille et al., 2020) is commonly found throughout the oceans. The monitoring and forecast of their trajectories are key to improving the efficiency of marine debris (Morrison et al., 2019) and *Sargassum* (Langin, 2018) removal efforts, search-and-rescue operations of different types (Breivik et al., 2013; Serra et al., 2020), and marine safety (Hong et al., 2017). However, forecasting the trajectories of floating matter is challenging due to a number of forcing agents controlling its motion.

Indeed, the well-established fluid mechanics′ Maxey-Riley equation (Maxey & Riley, 1983) dictates from first principles that a finite-size particle immersed in the flow of a fluid with possible different density—that is, an *inertial* particle—will be accelerated by the undisturbed fluid's flow force and added mass force (resulting from part of the fluid moving with the particle), while its trajectory may be deflected by shear-induced lift and Coriolis (in a geophysical fluid) forces and affected by the drag force (due to the fluid's viscosity). The effects of these forces prevent an inertial particle from adapting its velocity to that of the carrying fluid. In other words, inertial particle motion can be quite different than Lagrangian (i.e., fluid) particle motion (Cartwright et al., 2010).

In this letter we report on the analysis of trajectories produced by custom-made undrogued surface drifters designed to mimic floating marine debris of varied sizes and shapes and small patches of pelagic *Sargassum*. These special drifters were deployed together with conventional drifters at several locations along the path of the 2018 PIRATA (Prediction and Research Moored Array in the Tropical Atlantic) Northeast Extension cruise to study how marine debris and *Sargassum* move under different ocean and wind conditions (Duffy et al., 2019) and assess inertial effects on their drift. The motion of the drifters is investigated using a Maxey-Riley equation proposed by Beron-Vera et al. (2019)—henceforth referred to as *BOM equation*—as a first-principle-based alternative to ad hoc approaches commonly taken in oceanography to simulate the influence of ocean currents and winds on the drift of floating matter (Allshouse et al., 2017; Trinanes et al., 2016). This work extends the scope of the initial, successful testing of the BOM equation (Olascoaga et al., 2020) by considering various drifters of the same design type per deployment, which enabled to observe clustering of paths dominated by inertial effects. It also considers longer trajectories, which, sampling a wider range of ocean current and wind conditions, enabled a much more stringent test of the importance of inertial effects.

2. Methods

The trajectories of the drifters that are the focus of this letter are depicted in Figure 1. These trajectories were produced by 47 drifters specially designed at NOAA's Atlantic Oceanographic and Meteorological Laboratory. Five types of special drifters were built. The four debris-like drifters comprised a main body, made of polystyrene foam, and a short-weighted tube at the bottom. Two kinds of main bodies were considered: spherical (of two sizes) and cuboidal (a cube and a square cuboid). The volume of the tube was too small to significantly contribute to the buoyancy of the drifter. Rather, it ensured that the GPS (Global Positioning System) track devices were maintained above the sea level at all times, transmitting positions every 6 hr. The fifth special drifter type consisted of an artificial boxwood hedge designed to mimic a small patch of pelagic *Sargassum* (Olascoaga et al., 2020; Putman et al., 2020). The GPS tracker in this case was placed inside a small polystyrene foam cone inserted in the hedge. A total of 15 small spheres, 2 large spheres, 10 cubes, 8 square cuboids, and 12 hedges were produced. Figure 1 includes reference trajectories produced by eight additional drifters from NOAA's Global Drifter Program (Lumpkin & Pazos, 2009) with positions satellite tracked using GPS. Four of these drifters followed the conventional Surface Velocity Program (SVP) design with a spherical surface float and a drogue (holey sock) attached to it and centered at 15-m depth, which serves to minimize wind slippage and wave-induced drift (Sybrandy & Niiler, 1991). The other four SVP drifters had no drogue attached. Four deployments were carried out on 11, 14, 20, and 28 March 2018, each one involving more than one special drifter of each class, along with one drogued and one undrogued SVP drifter. The differences among drifters used in these experiments ensured that the studies could be done for a variety of buoyancy and drifter aerial exposure to winds.

The redundancy of special drifter types per deployment enabled a classification of the motion of the drifters as a function of inertial characteristics. This classification was carried out using the Kmeans clustering algorithm (Forgy, 1965; Lloyd, 1982). Given a number of points distributed in some space, the algorithm regroups the points into n clusters that minimize the square of the pairwise distance between points of a cluster (also known as the within-cluster sum-of-squares criterion). The parameter n was set to the a priori known number of distinct types of special drifters included in each deployment, that is, 4, 4, 4, and 3 for Deployments 1, 2, 3, and 4, respectively. Essentially the same results are obtained using unsupervised techniques such as DBSCAN (Density-Based Spatial Clustering of Applications with Noise) (Ester et al., 1996), which adds confidence to the results. Earlier works applying clustering algorithms to trajectory data include those of Froyland and Padberg-Gehle (2015) and Hadjighasem et al. (2017); however, transport barriers in the carrying flow can be bypassed by inertial particles (Beron-Vera et al., 2015).

Further insight into the motion of the drifters was attained by applying the BOM equation, which is formulated as follows. Consider a small spherical particle of radius a characterized by negligible air-to-particle density ratio and finite water-to-particle density ratio $\delta \geq 1$, loosely referred to as *buoyancy*, so reserve volume is well approximated by $1 - \delta^{-1} \in [0, 1)$ (Olascoaga et al., 2020). If the particle is not spherical, we treat it as if it was so, but with an effective radius $a\sqrt{3a_{\mathrm{v}}/(a_{\mathrm{n}} + a_{\mathrm{s}})}$, where a is the average of a_{n}, a_{s}, and a_{v}, which are the radii of the spheres with equivalent projected area, surface area, and equivalent volume, respectively. Let $\mathbf{x} = (x, y)$ denote position on the surface of the Earth, where $x = (\lambda - \lambda_0)a_{\odot} \cos\vartheta_0$ and $y = (\vartheta - \vartheta_0)a_{\odot}$ are northward and eastward local curvilinear coordinates, respectively, measured from
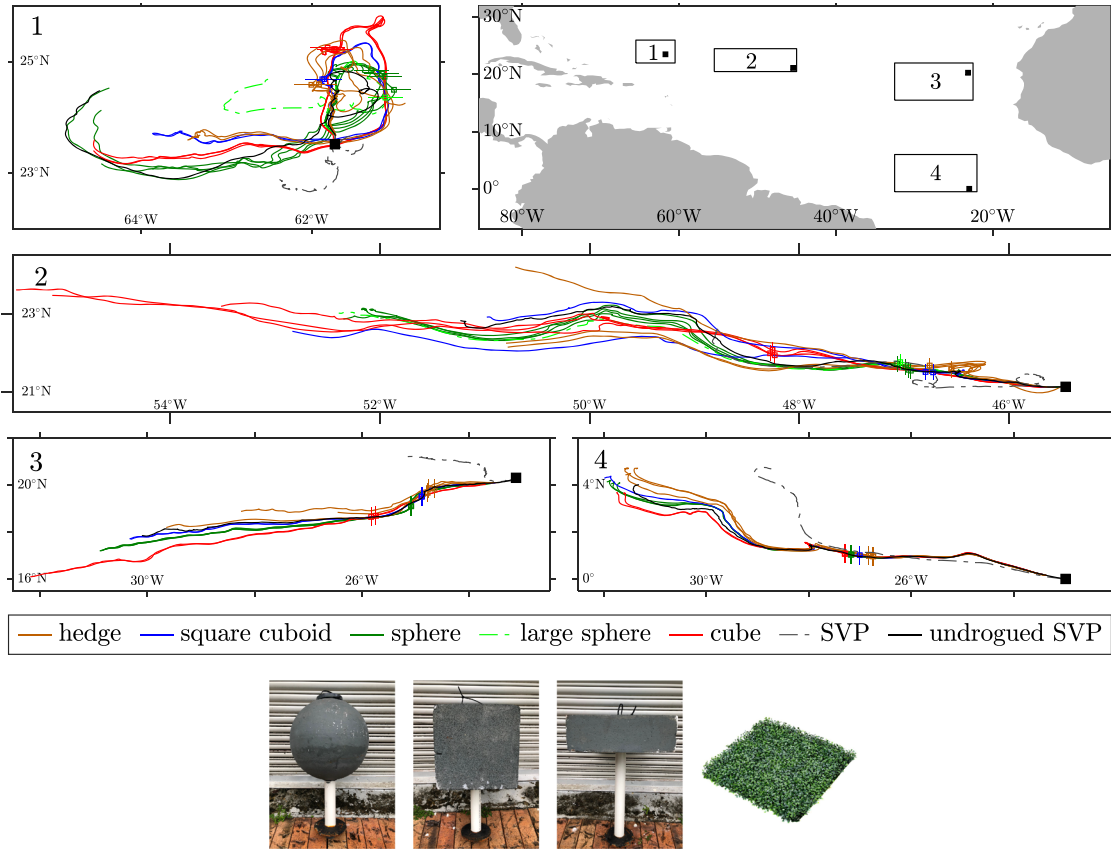
Figure 1. One-month-long trajectories of the five types of drifters deployed along the PIRATA Northeast Extension cruise in the North Atlantic on 11 (1), 14 (2), 20 (3), and 28 (4) March 2018. Trajectories produced by debris-like drifters (small spheres, large spheres, cubes, and square cuboids) and *Sargassum*-like drifters (hedges), which are represented as solid-green, dashed-green, solid-red, solid-blue, and solid-brown curves, respectively. Markers indicate positions of debris-like drifters 1 week after deployment. Dashed- and solid-black curves are trajectories of drogued and undrogued SVP drifters, respectively. The special drifters (excluding the large sphere) are displayed at the bottom.

(λ_0, ϑ_0), with λ (respectively, ϑ) longitude (respectively, latitude). Here $a_\odot$ is the Earth's mean radius, and $\gamma_\odot := \sec \vartheta_0 \cos \vartheta$ is a geometric factor (due to the planet's curvature) needed to compute distance; that is, $\gamma_\odot^2 dx^2 + dy^2 =: dx^\top m_\odot^2 dx$ gives the arc length square ($m_\odot$ is the metric matrix with $\gamma_\odot$ in the upper left entry and 1 in the lower right entry). The BOM equation provides a motion law for the particle in the form of a second-order ordinary differential equation given by (the overdot denotes time derivative)

$$\dot{\mathbf{v}}_p + \left(f + \tau_\odot v_p^x + \frac{1}{3} R \omega \right) \mathbf{v}_p^\perp + \frac{\mathbf{v}_p}{\tau} = R \frac{D\mathbf{v}}{Dt} + R \left(f + \tau_\odot v^x + \frac{1}{3} \omega \right) \mathbf{v}^\perp + \frac{\mathbf{u}}{\tau}, \tag{1}$$

where $\mathbf{v}_p = m_\odot \dot{\mathbf{x}}$ is the particle's velocity,

$$\mathbf{u} := (1 - \alpha)\mathbf{v} + \alpha \mathbf{v}_a, \tag{2}$$

and $\perp$ represents a $+\frac{\pi}{2}$ rotation.

Time- and/or position-dependent quantities in (1) and (2) are the (horizontal) velocity of the water, $\mathbf{v} = (v^x, v^y)$, where v^x (respectively, v^y) is zonal (respectively, meridional); its material (water-particle-following) derivative, $\frac{D}{Dt}\mathbf{v} = \partial_t \mathbf{v} + \gamma_\odot^{-1}(\partial_x \mathbf{v})v^x + (\partial_y \mathbf{v})v^y$; the water's vorticity, $\omega = \gamma_\odot^{-1} \partial_x v^y - \partial_y v^x + \tau_\odot v^x$, where $\tau_\odot := a_\odot^{-1} \tan \vartheta$; the velocity of the air, $\mathbf{v}_a$; and the Coriolis frequency, $f = 2\Omega \sin \vartheta$, where Ω is the planet's angular velocity magnitude.

Primary BOM equation's parameters a and δ determine secondary parameters α, R, and τ as follows: $\alpha := \gamma \Psi / (1 + (1 - \gamma)\Psi) \in [0, 1]$, which makes the convex combination (2) a weighted average of water and air velocities ($\gamma \approx 0.0167$ is the air-to-water viscosity ratio); $R := (1 - \frac{1}{2}\Phi)/(1 - \frac{1}{6}\Phi) \in [0, 1]$; and

Table 1
Parameters That Characterize the Special Drifters as Inertial "Particles"

	Parameter				
	Primary		Secondary		
Drifter	a (cm)	δ	α	R	τ [d^{-1}]
Small sphere	12.4	4.0	0.043	0.42	0.0008
Large sphere	14.0	5.5	0.058	0.36	0.0031
Cube	15.9	6.8	0.071	0.32	0.0002
Square cuboid	12.9	4.5	0.048	0.40	0.0006
Hedge	21.5	1.2	0.005	0.79	0.0320

$\tau := \frac{a^2\rho}{3\mu} \cdot (1 - \frac{1}{6}\Phi)/(1 + (1 - \gamma)\Psi)\delta^4 > 0$, which measures the *inertial response time* of the medium to the particle (ρ is the assumed constant water density and μ the water dynamic viscosity). Here $\Phi := \frac{i\sqrt{3}}{2}(\varphi^{-1} - \varphi) - \frac{1}{2}(\varphi^{-1} + \varphi) + 1 \in [0, 2)$ is the fraction of emerged particle piece's height, where $\varphi^3 := i\sqrt{1 - (2\delta^{-1} - 1)^2} + 2\delta^{-1} - 1$, and $\Psi := \pi^{-1}\cos^{-1}(1 - \Phi) - \pi^{-1}(1 - \Phi)\sqrt{1 - (1 - \Phi)^2} \in [0, 1)$, which gives the fraction of emerged particle's projected (in the flow direction) area.

Details of the derivation of the BOM equation are deferred to Beron-Vera et al. (2019) (cf. also Olascoaga et al., 2020, for an evaluation of its range of validity and a proposition for making the system self-consistent). Here we simply mention that it mainly follows from vertically integrating the original Maxey-Riley equation, adapted to account for the effects of the Earth's rotation and curvature, for a particle floating at an unperturbed air-sea interface. In particular, we note that (2), which plays an outstanding role in short-term evolution through its dependence on δ (buoyancy) as we will show, follows from integrating the (Stokes) drag term.

In the simulations discussed below, **v** in the BOM equation is taken as a daily surface velocity synthesis at 0.25° resolution of geostrophic flow derived from multisatellite altimetry observations (Le Traon et al., 1998) and Ekman drift induced from wind reanalysis (Dee et al., 2011), combined to minimize differences with velocities of drogued SVP drifters. Consistent with the geostrophic component of this **v** representation, we restricted our simulations to Deployments 1–3, which lie sufficiently away from the equator (cf. Figure 1). In turn, **v**$_a$ is taken as the same reanalyzed wind involved in the surface velocity synthesis. More precisely, **v**$_a$ is set to half the 10-m height reanalyzed wind (Hsu et al., 1994). These multidata-based mesoscale ocean currents and winds from reanalysis were shown capable of representing reality quite accurately in our first implementation of the BOM equation (Olascoaga et al., 2020). The specific values taken by the various (primary and secondary) inertia parameters for each of the special drifter types are shown in Table 1. These represent mean values (the weight of drifters of the same type typically vary about 1.5%), assuming an average climatological seawater density value of 1,025 kg m^{-3}. Integrations were carried out using Dormand and Prince (1980) scheme with interpolations (in space and time) done using a cubic method.

Finally, the Fréchet distance between observed and simulated trajectories was used to quantitatively assess the skill of the BOM equation. The Fréchet distance is the shortest cord length between two points traveling on separate curves, possibly at different speeds (Da Silva & Bozzelli, 2008). Previous studies (Olascoaga et al., 2020) have used other measures, such as the Hausdorff distance, which is the longest of all shortest distances between two curves. The conclusions we present here are not sensitive to a particular measure of curve similarity, as the Fréchet and Hausdorff distances produced indistinguishable results.

3. Results

We begin with a qualitative description of the observed trajectories (Figure 1). While the special and undrogued drifters exhibit diverse paths among themselves, they differ quite starkly from those taken by the drogued drifters. However, a quite evident aspect of the special drifter trajectories is a tendency to cluster according to type; that is, objects of a type are diverging at a slower rate than objects of other types. A single color is used to depict trajectories of special drifters of the same type in Figure 1. Note the relatively small spread of curves of the same color. This strongly suggests that inertial effects are dominant.
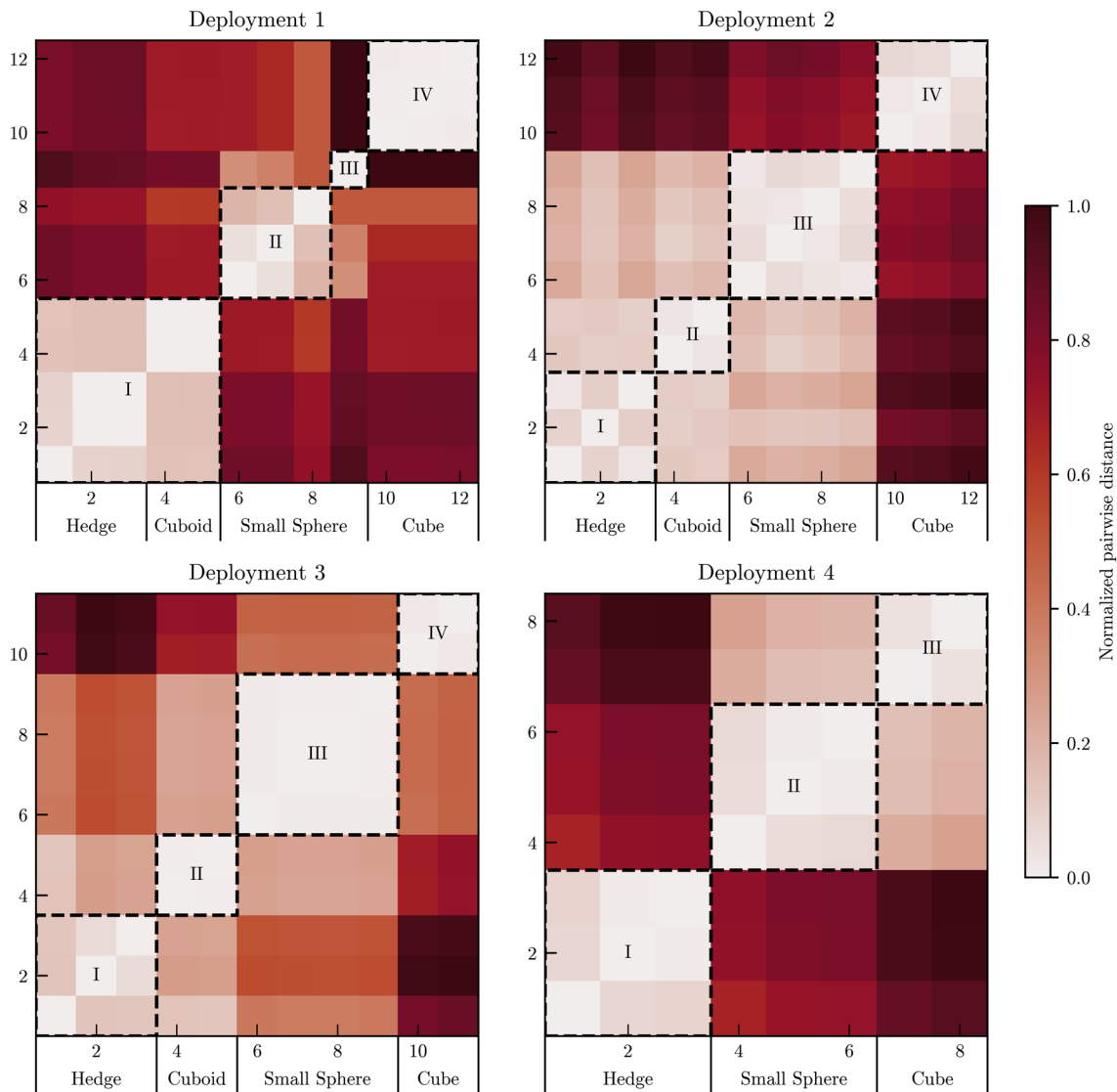
Figure 2. Normalized distance matrix (presented from white to red) between pairs of hedges, square cuboids, small spheres, and cubes, cumulative from deployment out to the end of the first week. Indicated by black squares and roman numerals are the clusters revealed by Kmeans analysis.

The above qualitative inference is quantified by constructing a matrix D with (i,j)th entry given by the distance between drifter pair $(i,j) \in I \times I$, cumulative from deployment until the end of the first week (I is the set of drifters in question). Clearly, $D_{ij} = 0$ for $i = j$. Figure 2 shows D for each deployment in Figure 1 with I grouped by special drifter type. Cursory inspection of Figure 2 reveals predominantly low values of D for drifters of the same type, irrespective of the deployment. This is seen more so by applying Kmeans clustering on the positions of the special drifters at the end of the first week (indicated in Figure 1). To visualize the clustering results, the drifters that form a cluster are highlighted by a dashed contour on the D plot in Figure 2 and identified with a roman numeral. The clusters correspond quite well with hedges, square cuboids, spheres, and cubes, respectively.

The exception is Deployment 1, in which case only cubes are identified as a well-defined cluster. Note that the clustering is not entirely determined by buoyancy (δ). Indeed, the cuboids ($\delta = 4.5$) tend to drift closer to the hedges ($\delta = 1.2$) than the small spheres ($\delta = 4$), as revealed by a systematically lower cumulative pairwise distance. Furthermore, the hedges and the cuboids are grouped into the same cluster (labeled I) in Deployment 1. This suggests that size and also (more likely) shape contribute to controlling the clustering. Overall, this quantitative clustering analysis supports the qualitative clustering assessment above.
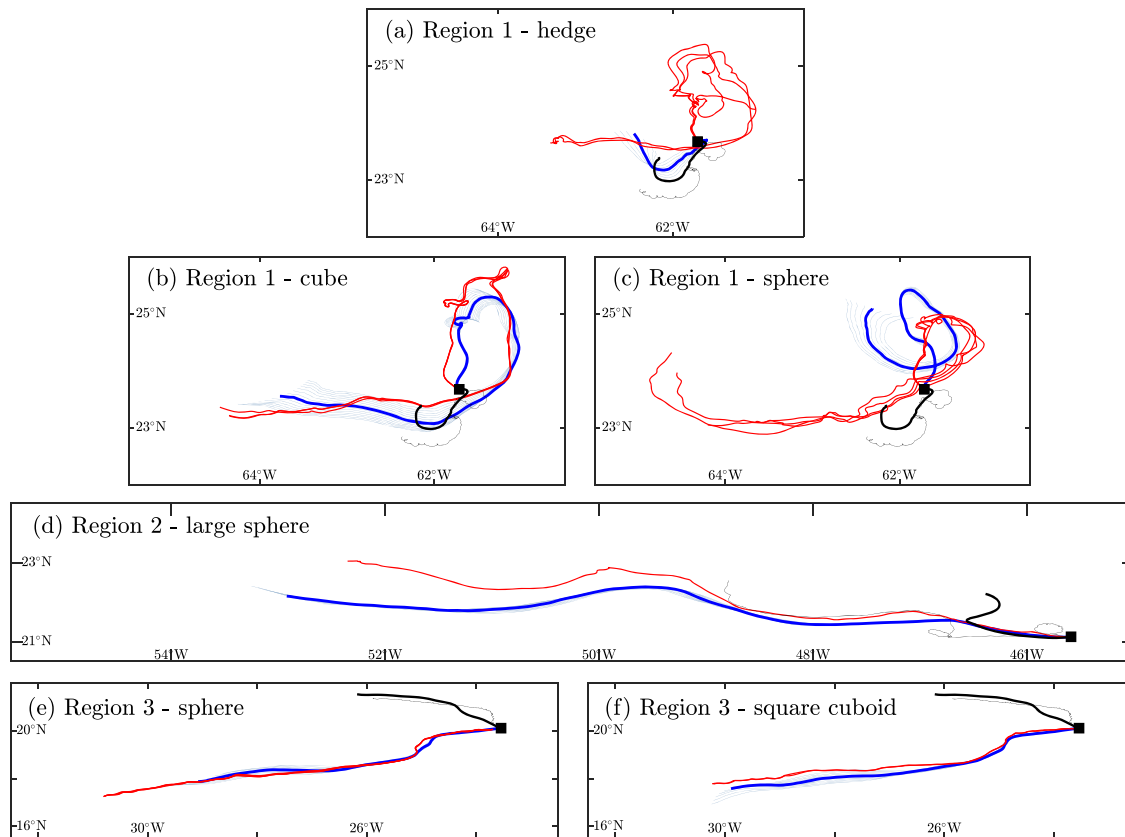
Figure 3. Observed (red) and BOM equation's (blue) 1-month-long trajectories corresponding to a hedge (a), cube (b), small sphere (c), large sphere (d), and square cube (e). Light blue curves are BOM trajectories with buoyancy allowed to vary 10% around its nominal value. Also shown in each panel is the trajectory of one drogued SVP drifter (thin black) and the trajectory produced by the altimetry/wind/drifter synthesis that provides a representation for the water velocity component of the BOM equation (heavy black). Deployment number and special drifter are indicated in each panel.

The observed clustering of the special drifters is explained, at large, by inertial effects as described by the BOM equation. This follows from the comparison of special drifter trajectories and trajectories produced by the BOM equation. As noted above, excluded from this assessment are trajectories from Deployment 4, which lie too close to the equator where the surface ocean current representation considered is not valid. Our assessment applies to all special drifters except hedges, which require a different description than that provided by the BOM equation. Meant to simulate pelagic *Sargassum* rafts, a minimal Maxey-Riley model for them would need to include elastic interactions between gas-filled bladders that keep rafts afloat. Such a minimal model has been proposed and applied with qualitative success (Beron-Vera & Miron, 2020). However, the hedges do not adhere to *Sargassum* rafts' morphology, and, thus, a different approach is needed. Indeed, they do not form networks of elastically interacting inertial particles but rather water-absorbing objects, which are not contemplated in the Maxey-Riley framework. In turn, differences between trajectories produced by solid special drifters and simulated counterparts can be attributed to uncertainties around inertia parameters (δ, primarily) but most likely to those around the carrying flow determination.

Representative examples of observed and BOM trajectories over a relatively long period of 1 month are presented in Figure 3. In all panels, red curves represent observed special drifter trajectories, while blue curves are corresponding BOM trajectories starting from observed initial positions and velocities. Included also are the trajectory of a drogued drifter (thin black) and a trajectory obtained by integrating $\dot{\mathbf{x}} = m_\odot^{-1}\mathbf{v}$ (recall that $\mathbf{v}$ is given by an altimetry/wind/drifter synthesis that is expected to most closely represent drogued drifter velocity). These examples sample the spectrum of successful, acceptably successful, not so successful, and mostly unsuccessful simulations. Beginning on the unsuccessful end, Panel (a) shows the typical situation with hedge drift simulation, which is invariably quite poor. Panels (b) and (c) provide examples of not-so-successful simulations, typically seen in Deployment 1. The cube trajectory (b) is reasonably well simulated, while the small sphere trajectory (c) is not, not even if δ is allowed to vary 10% around its nominal
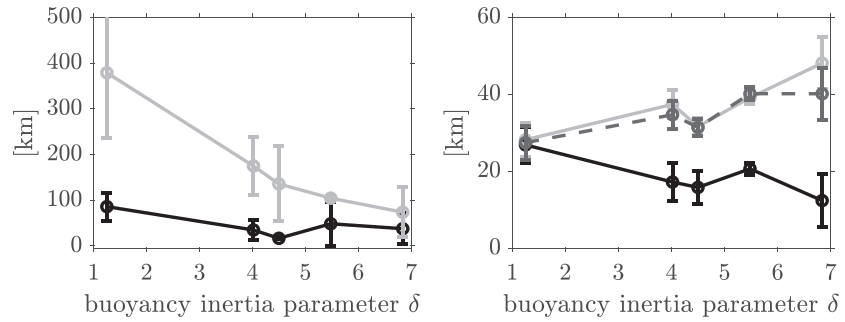
Figure 4. (left panel) As a function of buoyancy inertia parameter δ, the Fréchet distance between observed and BOM trajectories after 1 week (black) and 1 month (gray). Circles are mean values over all distances independent of deployment, while error bars are of one standard deviation across them. (right panel) Geodesic distance between observed and BOM positions after 1 day (black) along with that between observed position and simulated position based on the altimetry/wind/drifter ocean current synthesis (gray). The dashed curve is the mean distance traveled by the drifters in each group after 1 day since deployment.

value (light blue). Note that motion of the special drifters is quite different than that of the drogued drifter, which evidently is not completely described by the mesoscale ocean current synthesis, likely due in part to the smoothness of the gridded fields from the altimeter data used to derive geostrophic currents. Altogether ocean and wind representations in this region may be contributing to hinder the ability of the BOM equation to reproduce observed behavior (Putman et al., 2016). Panel (d) shows an example of acceptably successful simulations, typically seen in Deployment 2. Limitations of the ocean velocity representation, evidenced by its limited skill in reproducing the drogued SVP trajectory, appears to be a dominant factor in this case. Buoyancy variations about the nominal one for the large sphere do not contribute to reducing the differences with the observed trajectory that increase with time. Clearly, sensitivity to initial conditions and accumulated errors are important factors too in all cases. Finally, Panels (e) and (f) show typical examples of successful simulations for the case of a small sphere (e) and square cuboid (f), mainly happening in Deployment 3. These simulations reveal the importance of an accurate surface carrying flow representation (note the very good agreement in this case) between observed and simulated drogued drifter trajectories which contributes to enhancing the performance of the BOM equation. We note that the simulated trajectories in all cases are very similar to those resulting using the β-plane form of the BOM equation, which follows by setting, in (1), $\gamma_\odot = 1$, $\tau_\odot = 0$ and $f = f_0 + \beta y$ while treating $\mathbf{x}$ as Cartesian. This should be anticipated given their limited meridional extent (Ripa, 1997).

Quantitative assessments of the above qualitative assessments of the BOM equation's skill are presented in Figure 4. The left panel shows, as a function of buoyancy, the Fréchet distance between observed and BOM trajectories after 1 week (black) and 1 month (gray). While the variability can be large, the mean Fréchet distances are substantially much smaller for the square cuboids, cubes, and spheres than for the hedges, consistent with our qualitative assessments shown above. The Fréchet distances increase with time as can be expected. The right panel of Figure 4 shows, in a similar manner as in the left panel, the geodesic distance between observed and BOM position after 1 day (black) along with that between observed and simulated position based on the altimetry/wind/drifter ocean velocity synthesis (gray). The dashed curve, included for reference, is the mean distance traveled by the drifters in each group after 1 day since deployment. We have chosen 1 day as this is a critical time scale in search-and-rescue operations at sea (Breivik et al., 2013). Note that the BOM equation can improve the likelihood of such type of operations substantively.

We close this section by noting that BOM trajectories are very similar to those resulting by integrating $\dot{\mathbf{x}} = m_\odot^{-1}\mathbf{u}$. The reason for this is found in the relative smallness of the special drifters (equivalently, their short inertial response time τ). Indeed, application of geometric singular perturbation theory (Fenichel, 1979; Jones, 1995) extended to nonautonomous dynamical systems (Haller & Sapsis, 2008) on (1) and (2) reveals (Beron-Vera et al., 2019) that the trajectory of a sufficiently small inertial particle converges in the long run on an attracting *slow manifold* along which motion obeys $\dot{\mathbf{x}} = m_\odot^{-1}(\mathbf{u} + \tau\mathbf{u}_\tau)$, with an $O(\tau^2)$ error, where $\mathbf{u}_\tau := (R\frac{\mathrm{D}}{\mathrm{D}t}\mathbf{v} + R(f + \tau_\odot v^x + \frac{1}{3}\omega)\mathbf{v}^\perp - \frac{\mathrm{D}}{\mathrm{D}t}\mathbf{u} - (f + \tau_\odot v^x + \frac{1}{3}R\omega)\mathbf{u}^\perp$ with $\frac{\mathrm{D}}{\mathrm{D}t}\mathbf{u} = \partial_t\mathbf{u} + \gamma_\odot^{-1}(\partial_x\mathbf{u})u^x + (\partial_y\mathbf{u})u^y$. While this result is time asymptotic, initial behavior can be anticipated as follows. The slow manifold lies at an $O(\tau)$ distance from a *critical manifold* on which motion obeys $\dot{\mathbf{x}} = m_\odot^{-1}\mathbf{u}$.

Unlike the slow manifold, the critical manifold has no global effect on the dynamics of inertial particles controlled by (1) and (2). Yet, due to smooth dependence of solutions of the BOM Equations 1 and 2 on parameters, the trajectory of a sufficiently small particle will initially run close to the critical manifold if $\dot{\mathbf{x}}(t_0)$ is close to $(m_\ominus^{-1}\mathbf{u})(\mathbf{x}_0, t_0)$, before the particle starts to drift away from the critical manifold on its way toward the slow manifold. This observation is important in practice because the equations on the critical and slow manifolds do not require one to specify the velocity at the initial time (they are first-order equations), which is not known in general. It is clear, however, that long-term aspects of the inertial dynamics, such as the dynamics of great garbage patches (Beron-Vera et al., 2016, 2019) or mesoscale eddies as floating debris traps (Beron-Vera & Miron, 2020; Beron-Vera et al., 2015, 2019), cannot be described by the equation on the critical manifold. These are described by that on the slow manifold.

4. Conclusions

Two main conclusions were reached from the analysis presented in this letter. First, the trajectories of floating matter are strongly constrained by their buoyancy. This has been evidenced quite clearly from the analysis of the trajectories of custom-made undrogued drifters with varied designs, which revealed a tendency to cluster according to buoyancy and shape. In the case of objects, such as pelagic *Sargassum* patches and larger pieces of marine debris, assuming movement is strictly Lagrangian could have serious implications in our ability to forecast trajectories and conduct assessments of observed distribution patterns. This is particularly important for *Sargassum* as there is considerable uncertainty associated in determining the importance of localized growth versus long-distance transport on the inundation events in coastal areas throughout the Caribbean Sea (Brooks et al., 2019; Johns et al., 2020; Putman et al., 2018, 2020). The second important conclusion from our study is that the BOM equation, a recently proposed Maxey-Riley equation for the motion of finite-size particles floating on the ocean surface (Beron-Vera et al., 2019), provides a very reasonable explanation for the observed motion. We argued that uncertainties around the ocean current representation (the ocean velocity considered here did not represent submesoscale aspects of the motion, such as wave-induced drift) are the main factors contributing to departures from observed behavior. This inference finds additional support on controlled air-water stream flume experiments involving spheres of different buoyancies (Miron et al., 2020) that show that motion dependence on inertia characteristics (particularly drag dependence on buoyancy) is very well described by the BOM equation. Future studies may include laboratory experimentation aimed at better framing arbitrary shaped object motion and incorporating wave-induced drift, at present represented at the carrying flow level. Field experiments in a near-coastal area well sampled by high-frequency radars and weather stations involving actual debris pieces and *Sargassum* patches would be desirable to test the results of any improvements to this theory. An important final remark is that the physical mechanism of clustering described here—inertia—is different than that described in recent publications (D'Asaro et al., 2018; Huntley et al., 2015)—carrying flow compressibility—which, if active, would have affected all drifters equally, irrespective of their type.

Data Availability Statement

The trajectories are available online (at https://doi.org/10.17604/ckxq-nh63). The gridded velocity fields from the altimetry/wind/drifter synthesis can be obtained online (from https://www.aoml.noaa.gov/phod/gdp/gridded_velocity.php). The ERA-Interim reanalysis is available online (from https://apps.ecmwf.int/datasets/data/interim-full-daily).

References

Allshouse, M. R., Ivey, G. N., Lowe, R. J., Jones, N. L., Beegle-Krause, C. J., Xu, J., & Peacock, T. (2017). Impact of windage on ocean surface Lagrangian coherent structures. *Environmental Fluid Mechanics*, *17*(3), 473–483. https://doi.org/10.1007/s10652-016-9499-3

Beron-Vera, F. J., & Miron, P. (2020). A minimal Maxey–Riley model for the drift of *Sargassum* rafts. *Journal of Fluid Mechanics*, *904*, A8. https://doi.org/10.1017/jfm.2020.666

Beron-Vera, F. J., Olascoaga, M. J., Haller, G., Farazmand, M., Triñanes, J., & Wang, Y. (2015). Dissipative inertial transport patterns near coherent Lagrangian eddies in the ocean. *Chaos*, *25*(8), 087412. https://doi.org/10.1063/1.4928693

Beron-Vera, F. J., Olascoaga, M. J., & Lumpkin, R. (2016). Inertia-induced accumulation of flotsam in the subtropical gyres. *Geophysical Research Letters*, *43*, 12,228–12,233. https://doi.org/10.1002/2016GL071443

Beron-Vera, F. J., Olascoaga, M. J., & Miron, P. (2019). Building a Maxey-Riley framework for surface ocean inertial particle dynamics. *Physics of Fluids*, *31*(9), 096602. https://doi.org/10.1063/1.5110731

Breivik, O., Allen, A. A., Maisondieu, C., & Olagnon, M. (2013). Advances in search and rescue at sea, Topical collection on advances in search and rescue at sea. *Ocean Dynamics*, *63*(1), 83–88. https://doi.org/10.1007/s10236-012-0581-1

Brooks, M. T., Coles, V. J., & Coles, W. C. (2019). Inertia influences pelagic *Sargassum* advection and distribution. *Geophysical Research Letters*, *46*, 2610–2618. https://doi.org/10.1029/2018GL081489

Cózar, A., Echevarría, F., González-Gordillo, J. I., Irigoien, X., Úbeda, B., Hernández-León, S., et al. (2014). Plastic debris in the open ocean. *Proceedings of the National Academy of Sciences of the United States of America*, *111*(28), 10,239–10,244. https://doi.org/10.1073/pnas.1314705111

Cartwright, J. H., Feudel, U., Károlyi, G., De Moura, A., Piro, O., & Tél, T. (2010). Dynamics of finite-size particles in chaotic fluid flows. *Understanding Complex Systems*, *2010*, 51–87. https://doi.org/10.1007/978-3-642-04629-2_4

D'Asaro, E. A., Shcherbina, A. Y., Klymak, J. M., Molemaker, J., Novelli, G., Guigand, C. M., et al. (2018). Ocean convergence and the dispersion of flotsam. *Proceedings of the National Academy of Sciences of the United States of America*, *115*(6), 1162–1167. https://doi.org/10.1073/pnas.1718453115

Da Silva, G., & Bozzelli, J. W. (2008). Variational analysis of the phenyl $+ O_2$ and phenoxy $+ O$ reactions. *Journal of Physical Chemistry A*, *112*(16), 3566–3575. https://doi.org/10.1021/jp7118845

Dee, D. P., Uppala, S. M., Simmons, A. J., Berrisford, P., Poli, P., Kobayashi, S., et al. (2011). The ERA-Interim reanalysis: Configuration and performance of the data assimilation system. *Quarterly Journal of the Royal Meteorological Society*, *137*(656), 553–597. https://doi.org/10.1002/qj.828

Dormand, J. R., & Prince, P. J. (1980). A family of embedded Runge-Kutta formulae. *Journal of Computational and Applied Mathematics*, *6*(1), 19–26. https://doi.org/10.1016/0771-050X(80)90013-3

Duffy, J. E., Benedetti-Cecchi, L., Trinanes, J., Muller-Karger, F. E., Ambo-Rappe, R., Boström, C., et al. (2019). Toward a coordinated global observing system for seagrasses and marine macroalgae. *Frontiers in Marine Science*, *6*, 317. https://doi.org/10.3389/fmars.2019.00317

Ester, M., Kriegel, H.-P., Sander, J., & Xu, X. (1996). A density-based algorithm for discovering clusters in large spatial databases with noise. In *Proceedings of the 2nd International Conference on Knowledge Discovery and Data Mining* (pp. 226–231). https://doi.org/10.5555/3001460.3001507

Fenichel, N. (1979). Geometric singular perturbation theory for ordinary differential equations. *Journal of Differential Equations*, *31*(1), 53–98. https://doi.org/10.1016/0022-0396(79)90152-9

Forgy, E. (1965). Cluster analysis of multivariate data: Efficiency versus interpretability of classifications. *Biometrics*, *21*, 768–769.

Froyland, G., & Padberg-Gehle, K. (2015). A rough-and-ready cluster-based approach for extracting finite-time coherent sets from sparse and incomplete trajectory data. *Chaos*, *25*(8), 087406. https://doi.org/10.1063/1.4926372

Hadjighasem, A., Farazmand, M., Blazevski, D., Froyland, G., & Haller, G. (2017). A critical comparison of Lagrangian methods for coherent structure detection. *Chaos*, *27*(5), 053104. https://doi.org/10.1063/1.4982720

Haller, G., & Sapsis, T. (2008). Where do inertial particles go in fluid flows? *Physica D: Nonlinear Phenomena*, *237*(5), 573–583. https://doi.org/10.1016/j.physd.2007.09.027

Hong, S., Lee, J., & Lim, S. (2017). Navigational threats by derelict fishing gear to navy ships in the Korean seas. *Marine Pollution Bulletin*, *119*(2), 100–105. https://doi.org/10.1016/j.marpolbul.2017.04.006

Hsu, S. A., Meindl, E. A., & Gilhousen, D. B. (1994). Determining the power-law wind-profile exponent under near-neutral stability conditions at sea. *Journal of Applied Meteorology*, *33*(6), 757–765. https://doi.org/10.1175/1520-0450(1994)033<0757:DTPLWP>2.0.CO;2

Huntley, H. S., Lipphardt, B. L., Jacobs, G., & Kirwan, A. D. (2015). Clusters, deformation, and dilation: Diagnostics for material accumulation regions. *Journal of Geophysical Research: Oceans*, *120*, 6622–6636. https://doi.org/10.1002/2015JC011036

Johns, E. M., Lumpkin, R., Putman, N. F., Smith, R. H., Muller-Karger, F. E., Rueda-Roa, T. D., et al. (2020). The establishment of a pelagic *Sargassum* population in the tropical Atlantic: Biological consequences of a basin-scale long distance dispersal event. *Progress in Oceanography*, *182*, 102269. https://doi.org/10.1016/j.pocean.2020.102269

Jones, C. K. R. T. (1995). *Dynamical systems, lecture notes in mathematics*. In R. Johnson (Ed.), (Vol. 1609, pp. 44–118). Berlin: Springer-Verlag.

Langin, K. (2018). Seaweed masses assault Caribbean islands. *Science*, *360*(6394), 1157–1158. https://doi.org/10.1126/science.360.6394.1157

Le Traon, P. Y., Nadal, F., & Ducet, N. (1998). An improved mapping method of multisatellite altimeter data. *Journal of Atmospheric and Oceanic Technology*, *15*(2), 522–534. https://doi.org/10.1175/1520-0426(1998)015<0522:AIMMOM>2.0.CO;2

Lloyd, S. P. (1982). Least squares quantization in PCM. *IEEE Transactions on Information Theory*, *28*(2), 129–137. https://doi.org/10.1109/TIT.1982.1056489

Lumpkin, R., & Pazos, M. (2009). Measuring surface currents with Surface Velocity Program drifters: The instrument, its data, and some recent results, *Lagrangian analysis and prediction of coastal and ocean dynamics* (pp. 39–67). https://doi.org/10.1017/cbo9780511535901.003

Maxey, M. R., & Riley, J. J. (1983). Equation of motion for a small rigid sphere in a nonuniform flow. *Physics of Fluids*, *26*(4), 883–889. https://doi.org/10.1063/1.864230

Maximenko, N., Corradi, P., Law, K. L., Sebille, E. V., Garaba, S. P., Lampitt, R. S., et al. (2019). Towards the integrated marine debris observing system. *Frontiers in Marine Science*, *6*, 447. https://doi.org/10.3389/fmars.2019.00447

Miron, P., Medina, S., Olascoaga, M. J., & Beron-Vera, F. J. (2020). Laboratory verification of the buoyancy dependence of the carrying flow in a Maxey–Riley theory for inertial ocean dynamics. *Physics of Fluids*, *32*(7), 71703. https://doi.org/10.1063/5.0018272

Morrison, E., Shipman, A., Shrestha, S., Squier, E., & Stack Whitney, K. (2019). Evaluating The Ocean Cleanup, a marine debris removal project in the North Pacific Gyre, using SWOT analysis. *Case Studies in the Environment*, *3*(1), 1–6. https://doi.org/10.1525/cse.2018.001875

Olascoaga, M. J., Beron-Vera, F. J., Miron, P., Triñanes, J., Putman, N. F., Lumpkin, R., & Goni, G. J. (2020). Observation and quantification of inertial effects on the drift of floating objects at the ocean surface. *Physics of Fluids*, *32*(2), 26601. https://doi.org/10.1063/1.5139045

Putman, N. F., Goni, G. J., Gramer, L. J., Hu, C., Johns, E. M., Trinanes, J., & Wang, M. (2018). Simulating transport pathways of pelagic *Sargassum* from the equatorial Atlantic into the Caribbean Sea. *Progress in Oceanography*, *165*, 205–214. https://doi.org/10.1016/j.pocean.2018.06.009

Putman, N. F., Lumpkin, R., Olascoaga, M. J., Trinanes, J., & Goni, G. J. (2020). Improving transport predictions of pelagic *Sargassum*. *Journal of Experimental Marine Biology and Ecology*, *529*, 151398. https://doi.org/10.1016/j.jembe.2020.151398

Putman, N. F., Lumpkin, R., Sacco, A. E., & Mansfield, K. L. (2016). Passive drift or active swimming in marine organisms? *Proceedings of the Royal Society B: Biological Sciences*, *283*(1844), 20161689. https://doi.org/10.1098/rspb.2016.1689

Ripa, P. (1997). "Inertial" oscillations and the β-plane approximation(s). *Journal of Physical Oceanography*, *27*(5), 633–647. https://doi.org/10.1175/1520-0485(1997)027<0633:IOATPA>2.0.CO;2

Serra, M., Sathe, P., Rypina, I., Kirincich, A., Ross, S. D., Lermusiaux, P., et al. (2020). Search and rescue at sea aided by hidden flow structures. *Nature Communications*, *11*(1), 2525. https://doi.org/10.1038/s41467-020-16281-x

Sybrandy, A. L., & Niiler, P. P. (1991). WOCE/TOGA Lagrangian drifter construction manual. (*SIO Reference 91/6*). La Jolla, California: Scripps Institution of Oceanography. papers2://publication/uuid/6764775C-335F-4AC0-AB54-DA1264AEDFE2

Trinanes, J. A., Olascoaga, M. J., Goni, G. J., Maximenko, N. A., Griffin, D. A., & Hafner, J. (2016). Analysis of flight MH370 potential debris trajectories using ocean observations and numerical model results. *Journal of Operational Oceanography*, *9*(2), 126–138. https://doi.org/10.1080/1755876X.2016.1248149

Van Sebille, E., Aliani, S., Law, K. L., Maximenko, N., Alsina, J. M., Bagaev, A., et al. (2020). The physical oceanography of the transport of floating marine debris. https://doi.org/10.1088/1748-9326/ab6d7d